Nature Communications

https://doi.org/10.1038/s41467-026-73745-2

Article in Press

A self-powered spherical compound eye with 8 ns-motion response for source-constrained drones

Received: 10 January 2026

Accepted: 19 May 2026

Cite this article as: Ren, W., Zhao, X., Tang, J. *et al.* A self-powered spherical compound eye with 8 ns-motion response for source-constrained drones. *Nat Commun* (2026). https://doi.org/10.1038/s41467-026-73745-2

Wei Ren, Xiaoming Zhao, Jian Tang, Bohan Sun, Qingyi Meng, Lin Xiao, Qingqi Chen, Yang Shi, Zixi He, Ziyue Yang, Yu Zhou, Dangwu Ni, Liaoyong Wen, Bobo Tian, Xing Wu, Zhiyong Fan, Junhao Chu & Leilei Gu

Title: A Self-powered Spherical Compound Eye with 8 ns-motion Response for Source-constrained Drones

Author list: Wei Ren1†, Xiaoming Zhao2,3,4†, Jian Tang1, Bohan Sun1, Qingyi Meng1, Lin Xiao1, Qingqi Chen1, Yang Shi1, Zixi He1, Ziyue Yang1, Yu Zhou5, Dangwu Ni6, Liaoyong Wen6, Bobo Tian2,3,4*, Xing Wu7*, Zhiyong Fan5*, Junhao Chu2,3,4, Leilei Gu1,8,9*

Affiliations:

1Qingyuan Research Institute, School of Computer Science, Shanghai Jiao Tong University, Shanghai, China.

2Key Laboratory of Polar Materials and Devices, Ministry of Education, East China Normal University, Shanghai, China.

3Shanghai Center of Brain-inspired Intelligent Materials and Devices, East China Normal University, Shanghai, China.

4Shanghai Key Laboratory of Multidimensional Information Processing, East China Normal University, Shanghai, China.

5Department of Electronic and Computer Engineering, The Hong Kong University of Science and Technology, Clear Water Bay, Kowloon, Hong Kong, China.

6Zhejiang Key Laboratory of 3D Micro/Nano Fabrication and Characterization, School of Engineering, Westlake University, Hangzhou, China.

7In Situ Devices Center, School of Integrated Circuits, East China Normal University, Shanghai, China.

8Shanghai Artificial Intelligence Laboratory, Shanghai, China.

9National Key Laboratory of Advanced Micro and Nano Manufacture Technology, Shanghai Jiao Tong University, Shanghai, China.

*Corresponding author. Email: bbtian@ee.ecnu.edu.cn, xwu@ee.ecnu.edu.cn, eezfan@ust.hk, leilei.gu@sjtu.edu.cn

†These authors contributed equally to this work.

Abstract:
Ultrafast dynamic vision remains a major challenge for autonomous systems like drones, particularly considering their strict power and computational constraints. Here, we present an artificial spherical compound eye (ASCE) that enables nanosecond-scale, event-driven motion detection across a panoramic field of view (294°). Each pixel is self-powered and responds exclusively to dynamic light changes, enabling real-time sensing with minimal processing. An 8 ns response time is achieved under femtosecond laser excitation, alongside exceptional stability exceeding 10^8 switching cycles. In addition, the ASCE features a simple structure with in situ grown nanowires and dielectric layer. The one-step fabrication process allows for conformal pixel integration on spherical and other three-

dimensional surfaces. We demonstrate its versatility across multi-scale applications, including drone-based laser alarming and real-time motion tracking. These results establish ASCE as a promising platform for energy-efficient, high-speed vision in autonomous robotics and intelligent surveillance.

Introduction:

Motion detection is vital for drones in tasks such as surveillance, delivery, and search-and-rescue tasks. Conventional visual systems, using cameras with compact deep learning models, offer onboard processing but suffer from slow response (20 – 50 ms)1,2. The stringent energy and computational constraints prevent the use of large visual models on the drone platforms. Further enhancing detection accuracy and latency, while simultaneously reducing size and power consumption, remains a major challenge. Combining the efforts in both data acquisition and processing can be an efficient way to tackle this challenge. Flying insects offer compelling biological inspiration. Their quasi-spherical compound eyes enable near-360° panoramic vision, and the local, parallel processing within ommatidia enables real-time motion tracking in complex environments3,4. These features highlight the promise of bioinspired vision systems for agile, low-power perception in autonomous drones.

A wide field of view (FoV) is essential for fast visual response, enabling earlier target detection across broader scenes. Conventional methods to expand FoV, however, often introduce trade-offs. Mechanical scanning increases system complexity, bulkiness, and latency, while highly curved optics, such as fisheye lenses, microlens arrays and waveguides, extend coverage without moving parts but can cause distortion and blurring due to the mismatch with planar sensors5–8. Correcting these artifacts requires computational post-processing, which adds latency and reduces temporal resolution9–11. The integration of curved photodiode arrays with spherical lenses utilizes a straightforward optical configuration that effectively minimizes distortion under large FoV conditions12,13. By contrast, a well-integrated three-dimensional sensor architecture can achieve wide-angle vision without such drawbacks, while more closely mimicking the panoramic and low-latency vision of biological compound eyes. Notable examples include deformable silicon mesh-based arrays14,15, biomimetic hemispherical nanowire architectures16,17 and other stretchable soft electronic devices18,19. These devices have demonstrated onboard real-time motion tracking, proving their application potential in drones and robotics14,17,20. However, their FoV remains far from the near-360° panoramic vision achieved by their natural counterparts14–19.

Fast and efficient data processing is another critical issue for high-speed motion perception. Insects achieve this via ommatidia that respond to light changes within 5 ms21, which is almost one order of magnitude faster than human vision22. In contrast, conventional frame-based sensors operate at fixed frame rates (typically 30–60 fps), producing redundant data and limiting temporal resolution23. Dynamic vision sensors (DVS), which is also known as silicon retina, offer a neuromorphic alternative by detecting only changes in light intensity, generating sparse, asynchronous signals with microsecond precision and low energy consumption24–26. Their utility in drone-based applications has been demonstrated, underscoring their potential for low-latency and power-efficient vision27–

29. However, existing dynamic vision sensor (DVS) devices rely on complex pixel architectures with analog peripheral circuits, which reduce fill factor, enlarge the pixel footprint, and hinder integration on non-planar or curved surfaces24,30–32. Extensive research efforts on materials and device design have been carried out to improve DVS architecture. Fernández-Peramo et al. replaced the conventional logarithmic transducer with a single photovoltaic diode, reducing noise and improving latency and power performance33. Zhou et al. developed an event sensor using only two oppositely polarized photodiodes34, while Feng et al. introduced a ferroelectric differentiator for efficient event-based sensing35. These advances lay the foundation for compact, high-performance, and conformable event-driven vision systems suitable for robotics, autonomous vehicles, and wearable technologies. However, it is still challenging to integrate DVS onto spherical surface due to its complex structure.

Herein, we report a nanowire-based spherical artificial compound eye that combines an ultrawide FoV with event-driven, self-powered pixels for nanosecond-scale motion detection. The spherical structure provides a wide FoV of 294°, enabling panoramic vision. The pixels respond exclusively to dynamic light changing, enabling hardware-level edge extraction and motion capture with minimal computational overhead. 8 ns response time is achieved by femtosecond laser excitation under 0 V bias voltage. The pixels also exhibit high stability, achieving over 10^8 continuous switching cycles, which is the highest reported for perovskite devices. This unique performance is attributed to an in situ formed Al_2O_3 layer at the nanowire base during chemical vapor deposition (CVD) growth. The one-step fabrication supports conformal integration on curved surfaces, addressing a key challenge in bioinspired vision. To prove its application potential, we have carried out multilevel demonstrations including a single pixel-based edge extraction and motion detection, a four-quadrant drone alarm system, and a 103-pixel array recording the motion of a car. This architecture offers a paradigm for energy-efficient, real-time vision in autonomous robotics and surveillance.

Results:

Overall device design

Figure 1a(i–iii) schematically illustrates the visual pathway of a dragonfly during prey capture, comparing the biological compound eye with our artificial counterpart. As shown in Fig. 1a(ii), the natural compound eye features a quasi-spherical geometry and performs motion detection through an array of elementary motion detectors (EMDs)36–38. These EMDs implement time delays and signal modulation directly in hardware, enabling fast motion processing at the edge—that is, locally and in real-time, without relying on centralized computation. This approach produces an analog output waveform proportional to motion velocity, forming a low-power neural processing architecture that minimizes the computational burden on the insect brain.

Similarly, the artificial spherical compound eye (ASCE), presented in Fig. 1a(iii), adopts a spherical architecture that enables real-time motion encoding directly at the sensor level. This geometry arises from a spherical Aluminum (Al) substrate, onto which a conformal anodic aluminum oxide (AAO) template is grown. Perovskite nanowires are then in situ grown within the template, forming high density and spherically aligned nanowire arrays. Top electrodes are further prepared, defining the pixel layout. Each pixel generates transient photocurrent spikes in response to abrupt light intensity changes, even under zero external bias. Spikes are positive for increasing light, negative for decreasing light, and zero under steady illumination. The spike amplitude reflects the magnitude of illumination change, allowing estimation of motion speed, while the motion direction selectivity is extracted from the event sequence of pixels, specifically the appearance and disappearance of events. Owing to the ultrafast device response, the paired positive/negative events occur with very short latency, enabling rapid direction estimation. This built-in neuromorphic response enables event-driven edge and motion sensing at the hardware level, making the system highly suitable for low-power, energy-efficient vision applications. Beyond its unique function, the device offers significant fabrication and structural advantages. It features a simplified architecture composed of CVD-grown perovskite nanowires and thermally evaporated top electrodes. The characteristic spike response originates from the residual Al_2O_3 layer (3–5 nm thick) formed naturally during template fabrication. This streamlined process eliminates the need for complex lithography or multilayer assembly, enabling scalable, low-cost fabrication, which is especially beneficial for three dimensional (3D) or non-planar surfaces. Notably, the AAO template can be readily fabricated on aluminum substrates of arbitrary geometry, making this approach a generalizable strategy for devices on curved or irregular surfaces. More details on the device can be found in the following sections.

Figure 1b(i) presents a photograph of the ASCE device, with a potential application scenario presented in Fig. 1b(ii). The device is mounted on a drone for real-time traffic flow monitoring. The self-powered property and ultrawide FoV enable a full-time and broad surveillance observation range. Figure 1b(iii) shows a representative output frame from this traffic monitoring scenario. Owing to its event-driven nature, the device responds only to the targets, the moving vehicles, while the other information about the static background elements such as trees, roads, and buildings are inherently filtered out at the hardware level. This sparse output offers several advantages, including efficient motion feature extraction, low power consumption and enhanced privacy, making it particularly suitable for continuous, long-term surveillance in energy-constrained environments.

Photoresponse characterization of individual pixel

Figure 2a presents the photo of an artificial compound eye mounted on a printed circuit board (PCB) ready for testing, with an additional exploded view shown in Supplementary Fig. 1a. The photosensitive sphere is surrounded by the optical components. Two covers are needed to enable full coverage, corresponding to an overall wide FoV. Each optical component consists of a pair of pinhole and lens (Supplementary Figs. 1b and c). A higher pinhole aspect ratio narrows the ommatidial FoV, improving angular selectivity, but reduces photon throughput and decreases overlap between neighboring ommatidia. The lens size and curvature affect the acceptance angle, per-pixel coverage, and working distance. Adding a small lens can boost light collection and improve responsivity and effective angular resolution of individual pixel, while the lens array influences the overall objective/working range. The lens focal length has to match with the thickness of pinhole to enable light incidence.

For the inner photosensitive sphere, the aluminum base acts as a common bottom electrode and the top electrodes define pixel positions. Pixels are arranged in a latitude-longitude grid, with 103 active pixels in total. Thin Cu wires (50 µm) embedded in flexible printed circuits (FPCs) route signals along longitude lines to the PCB.

The photoresponse of individual pixels is characterized to evaluate the effective FoV of the device. A group of optical pulses (470 nm, 3 mW/cm²), generated by a digital micromirror device (DMD), is used as the incident stimulus. As shown in Fig. 2b(i), along the vertical meridian of the sphere, indicated by the blue path in Fig. 2a, the pixels exhibit strong photoresponse except in the region spanning -30° to 30°, where no pixels are present because of wire routing. From the distribution of pixels, the FoV is estimated to be 294°, enabling non-scanning panoramic coverage. In addition, along the equatorial direction (red path in Fig. 2a), the device shows uniform photoresponse with current ranging from 200 to 300 nA across all pixels. This homogeneous output indicates full 360° coverage in the horizontal plane, confirming omnidirectional sensing capability around the equator (Fig. 2b(ii)). The extended FoV allows early target detection over a wide angular range, which is critical for applications such as autonomous navigation and surveillance. The spherical geometry is key to achieving an extended FoV. Adjusting the sphere's curvature directly changes ommatidial alignment, providing a straightforward design handle to tune the overall FoV and foveated vision.

Figure 2c presents the event-driven photoresponse of individual pixels. As shown in Fig. 2c(i), a representative I-t curve reveals a transient positive photocurrent pulse upon light onset, which rapidly decays to ~0 A as illumination stabilizes. Upon cessation of light, a transient negative photocurrent is generated. A key distinction of our device lies in its sensitivity to dynamic light modulation, with the photocurrent response governed by the rate of change in light intensity. Under fixed chopping frequency, the peak photocurrent increases with higher light intensity variations (Fig. 2c(ii)). Under constant light intensity, the response rises with increasing chopping frequency (Fig. 2c(iii)). In both cases, the peak response scales with the temporal gradient of the light stimulus, underscoring the device's ability to detect dynamic lighting conditions in real time. This behavior is in stark contrast to conventional photodetectors, which often yield stable or even diminished output at higher modulation rates39–41. Interestingly, when the optical pulse frequency is tuned by DMD, the device exhibits a constant photoresponse (Fig. 2c(iv)). To reveal this response difference, we have explored the profiles of optical pulses generated by chopper and DMD. As shown in Supplementary Figs. 2a and b, increasing the modulation frequency of the optical chopper reduces both the rising/falling time and pulse width. However, pulses modulated by the DMD exhibit fixed edge durations—determined by micromirror switching speed—while varying only in width. Correlating these optical profiles with the corresponding photocurrent responses reveals that the device is primarily activated by the edge dynamics, underscoring its motion-sensing and event-driven nature.

Figure 2c(v) summarizes the photoresponse of individual pixels as a function of incident light intensity, with the light transition rate fixed by the DMD. In general, higher intensities corresponding to high changing rate, yield larger peak photocurrents and faster response. The sensor can detect sub-microwatt light of 0.945 μW/cm², albeit with a relatively long response time (defined as t_{90}) of 2.8 ms. The pixel exhibits high specific detectivity of 6.18×1014 Jones, arising from its low dark current. As the light intensity increases to 9.27 mW/cm², the response time decreases dramatically to just 9.5 μs. The inset I-t curves at the lowest and highest illumination levels clearly show the photoresponse difference. Note that the measured response time of 9.5 μs closely approaches the intrinsic optical transition time of the DMD (~10 μs)42, suggesting that the sensor's true response speed may be limited by the modulation source rather than the device itself. To probe the intrinsic temporal resolution, we employ ultrashort femtosecond laser pulses with a pulse width of 300 fs (Supplementary Fig. 2c), enabling characterization of the sensor's fundamental speed independent of external modulation constraints. In this setup, the measurement approach is also adapted to enable higher temporal resolution. The current meter is replaced with a high-speed oscilloscope and the voltage is recorded as the output signal. Under excitation, the sensor exhibits an ultrafast rising time of just 8 ns, highlighting its exceptional dynamic performance (Fig. 2c(vi)). Note that in this case, the voltage generated across the detector terminals alters its capacitance, and therefore may introduce additional RC delay, slowing the measured response speed. An improved setup with ultrafast transimpedance amplifier connecting to an oscilloscope would benefit to minimize this effect.

Additional details regarding to this measurement protocol are provided in Supplementary Methods. Commercial event cameras offer sub-microsecond latency and can capture light intensity changes in the microwatt range30,31,43–50. Our pixel achieves nanosecond-level rapid response without complex circuitry, resulting in a higher fill factor and more powerful motion capture ability. Comparison of our pixel and the commercial DVS pixel is presented in Supplementary Fig. 3. In addition, the device exhibits a broadband photoresponse spanning the entire visible spectrum (Supplementary Figs. 4a and b), owing to the narrow bandgap of the $MAPbI_3$ perovskite material.

To illustrate this property more vividly, we demonstrate two representative scenarios: 1) edge extraction, corresponding to spatial variations in light across adjacent pixels, and 2) motion capture, representing temporal changes in light at the same pixel. Figure 2d(i) presents the schematic of the single-pixel scanning setup used to evaluate these dynamic responses. For edge extraction, the pixels are sequentially projected onto the device via the DMD, with bright pixels triggering illumination and dark ones not. The photocurrent spikes occur only at transitions between bright and dark pixels. Scanning all pixels produces a sparse matrix of current peaks, which are the edges that can be used to reconstruct the image. As shown in Fig. 2d(ii), the result emphasizes only the edges, demonstrating effective hardware-level edge extraction. More examples are demonstrated in Supplementary Fig. 5. For motion capture, the experimental setup remains the same, with the key difference being that a video stream is used as the input. Instead of scanning pixels in a static image, the brightness variation of each pixel over time is monitored. The spikes of all the pixels are assembled into a three-dimensional matrix that captures the spatiotemporal evolution of pixel brightness, enabling video reconstruction. Figure 2d(iii) presents representative frames from both the original and reconstructed videos, indicating that only moving parts are recorded. Supplementary Fig. 6 shows the full frames and the Supplementary Movie 1 provides the full reconstructed sequence, further demonstrating this trend. As observed, only regions exhibiting temporal brightness variation are captured, effectively highlighting the motion information. These unique capabilities, rooted in the device's intrinsic sensitivity to spatiotemporal light fluctuations, offer a low power, hardware-efficient strategy for visual analysis, making it particularly well-suited for lightweight edge devices such as drones and robots. Moreover, the pixels show high uniformity in photoresponse across a single device and small batch-to-batch variation, benefiting from the conformal growth of bottom Al2O3 layer and nanowires (Supplementary Fig. 7).

Fundamental mechanism for the exclusive motion response

To elucidate the underlying mechanism, we performed systematic Technology Computer-Aided Design (TCAD) simulation, complemented by experimental validation. Figure 3a(i) schematically illustrates the overall device geometry, while Fig. 3a(ii) highlights a single nanowire (NW) unit, which can be taken as the fundamental detection element. Each detection unit consists of a perovskite nanowire, a thin bottom Al_2O_3 layer, a bottom Al electrode, and a top ITO electrode. The Al_2O_3 layer functions as a capacitor dielectric in series with the nanowire resistance, forming a resistive-capacitive (RC) delay circuit that governs the transient photocurrent response (Fig. 3a(ii)). Upon illumination, photogenerated carriers charge the capacitor, resulting in a positive current spike. As the capacitor approaches saturation, the current decays to zero. When the light is turned off, the capacitor discharges, producing a negative current spike. Mott-Schottky measurements reveal that for a device with a 3.14 mm^2 area, the capacitance increases from ~0.2 nF to ~1.3 nF as light intensity rises from 0 to 9.26 mW cm^{-2} (Supplementary Fig. 8). Given a fixed pitch of 500 nm, this area of 3.24 mm2 contains 1.45 × 107 NWs. Therefore, the capacitance of individual NW can be estimated as 0.01–0.08 pF. The small capacitance is a key factor enabling a short RC delay, thereby leading to ultrafast photoresponse.

To verify this mechanism, a 2D model is employed for simulation to analyze the device behavior. The simulation details can be found in Supplementary Methods, with the device structure and parameters presented in Supplementary Fig. 9. The TCAD simulation clearly shows that the model incorporating the Al_2O_3 layer exhibits significantly greater hole accumulation during charging than the one without, underscoring the critical role of the bottom Al2O3 dielectric layer in modulating charge dynamics (Fig. 3a(iii)). This effect is further experimentally evidenced in Fig. 3b(i) and (ii). The device exhibits normal spiky response with bottom AAO layer. Upon removal of the Al_2O_3 layer via Ar^+ ion milling, the device exhibits a steady photoresponse, consistent with conventional sensors51. The morphology of the nanowires before and after ion milling are shown in Supplementary Fig. 10. A regrowth of perovskite is needed to fix the crystal damage from ion milling, which can eliminate the interference from trap states.

In addition to modulating charge dynamics, the carrier accumulation also affects the ions. It generates an electric field that opposes the built-in field, thereby suppressing ion migration (Fig. 3c(i)), which is a primary cause of degradation in perovskite-based devices52. This contributes to the device's exceptional stability: under continuous illumination (30 mW cm^{-2}) and 100 Hz chopping, it operated for 1.2×10^8 cycles (336 hours) without measurable degradation (Fig. 3c(ii)). To our best knowledge, this represents the most rigorous long-term stability test reported for perovskite sensors to date53–57. By contrast, an identical device operated under a 5 V external bias degraded after only 4×10^5 cycles, a three-order-of-magnitude difference in reproducibility (Supplementary Fig. 11). In addition, unlike conventional metal-insulator-metal devices, which often exhibit accumulative synaptic effects, featured as progressive current buildup under repeated stimuli58–61, our device maintains consistent output with repeating cycles. This stability stems from the suppressed ion migration and the presence of an ultrathin (~3 nm) Al_2O_3 layer, which is too thin to store mobile ions. The suppressed ion migration, along with 3D passivation from the surrounding AAO structure (Supplementary Fig. 12), ensures reliable and long-term operation.

A unique property of our device is that it exhibits stronger response to faster light stimuli. We performed additional TCAD simulations to elucidate the mechanism underlying the interesting property. As shown in Fig. 3d(i), under a fast-rising (0.1 μs) optical pulse, the photocurrent increases steadily throughout the rising edge. In contrast, a slower (1 μs) pulse leads to early saturation, resulting in a peak current nearly half that of the fast pulse. This trend is consistent with experimental observations. To further reveal the mechanism, the response processes are divided into four steps t1–t4, corresponding to the time when the light intensity is 25%, 50%, 75% and 100% of full light, respectively. As shown by the solid curves in Supplementary Fig. 13, the photogeneration rates for both fast and slow pulses are nearly identical. However, the slow pulse results in greater hole accumulation compared to the fast pulse, leading to a more pronounced suppression of the resulting photocurrent (dash curves in Supplementary Fig. 13). Particularly at t4, when the maximum difference in hole accumulation is arrived, the device exhibits peak photocurrent difference (Fig. 3d (ii and iii)). This effect is further visualized in Supplementary Figs. 14 and 15, which present contour maps of photogeneration rate and charge accumulation during the rising phase for both cases. These findings indicate that the device's transient response arises from a temporal mismatch between rapid photogeneration and slow charge accumulation. Faster stimuli limit charge buildup, reducing suppression and yielding a stronger photocurrent. This intrinsic characteristic makes our sensor particularly well-suited for ultrafast dynamic vision applications. Note that in this device, the effect of bottom Al2O3 is to promote interfacial charge accumulation, producing a transient, spike-like photoresponse. This is different from Al2O3 in other perovskite devices, although they have similar material system62.

Artificial spherical compound eye-based end-to-end emergency alarming for a drone

The device's combination of ultrawide FoV, fast response, and high energy efficiency makes it ideally suited for long-duration surveillance. Herein, we developed an onboard alarming system that enables a drone to detect and evade laser-based threats. As shown in Fig. 4a, the bioinspired design operates in an idle state with near-zero power consumption. Upon laser detection, the corresponding pixel generates a positive pulse, which is directly converted into actuator control signals, triggering an immediate evasive response. The 3D geometry of the compound eye gives each pixel a unique spatial orientation, allowing the system to detect both the presence and direction of incoming threats with minimal computation. Structurally, the system echoes the decentralized neural architecture of a dragonfly's ventral nerve cord63,64. While the anterior ganglia (brain) control head functions, the segmental ganglia govern the rest of the body independently, enabling reflexive, low-latency responses.

Figure 4b shows a photograph of a drone equipped with the integrated visual sensing system. The spherical eye is mounted on FPC (Supplementary Fig. 16a), whose output is connected to the microcontroller to control the propellers. To achieve small system latency, the circuit is designed to comprise four independent circuits, each responsible for monitoring a distinct direction. The data from these four independent channels are read simultaneously. Under this configuration, the system latency is primarily determined by the per-channel latency, rather than by multiplexing across pixels. One-channel circuit schematic is shown in Supplementary Fig. 16c. Incorporating more reading channels can increase more accurate directional information. However, it will also add the circuits complexity. The accuracy and complexity have to be well balanced. When the laser beam strikes the device, a positive pulse is generated at the specific channel, which changes the rotating speeds of the propellers, triggering the drone's corresponding evasive maneuver (Fig. 4c(i)). The drone continues to move away from the beam until the system detects a return to low voltage level, indicating the absence of the stimulus. The hardware sensor-to-actuator enables response with low latency and power consumption. The system employs decoupled charging and discharging pathways. This results in an asymmetric output profile characterized by a fast-rising edge for immediate activation and a slow-falling edge that prolongs the escape duration. The extended decay acts as a safety buffer, preventing premature termination of the escape behavior. Supplementary Fig. 16b illustrates the input-output timing sequence, highlighting the dynamic characteristics of the circuit. It exhibits an ultrashort reaction time of just 8 μs (Fig. 4c(ii)). This performance significantly surpasses that of state-of-the-art alarm systems of 3.5–20 ms, which typically rely on software-based processing and exhibit longer latencies1,20,27.

An on-ground demonstration of the system's function is provided in Supplementary Movie 2, with two representative frames shown in Fig. 4d(i and ii), respectively. As illustrated, different motors are selectively activated depending on the direction of the incoming beam, demonstrating the system's directional sensitivity. An in-flight demonstration is further presented in Fig. 4d(iii) and Supplementary Movie 3. During actual flight tests, the system reliably executes evasive maneuvers in response to hazardous light stimuli from all four directions. Upon withdrawal of the threat, the drone autonomously returns to a stable hover state, demonstrating robust threat detection and recovery behavior.

Note that the event-driven nature enables excellent system robustness by allowing the device to distinguish the response features of laser threats from typical environmental variations. Supplementary Figure 17 and Movie 4 present representative responses under interference conditions. For more complex real-world scenarios, additional sensors (e.g., an RGB camera and IMU) and advanced AI-based algorithms can be integrated to compensate for dynamic backgrounds and ego-motion29.

Artificial spherical compound eye-based fast motion tracking on a drone

To highlight the dynamic and panoramic vision of the ASCE, we demonstrate its capability for real-time motion tracking, leveraging all 103 pixels. As shown in Fig. 5a, a toy car moves across a table while an ASCE is mounted above, monitoring its surroundings. This setup mimics the scenario illustrated in Fig. 1b(ii), where the system is integrated onto a UAV for traffic surveillance. A light source mounted on the car provides dynamic illumination during movement. As the car moves, its light sweeps across the ommatidia, generating transient photocurrent spikes in response to changing light stimuli. Each pixel is connected to a dedicated Source Measurement Unit (SMU) channel. Totally, 103 channels are utilized, enabling simultaneous, high-speed readout of all the 103 pixels. Further experiment setup details are shown in Supplementary Fig. 18.

Figure 5b(i) presents the I-t curves recorded from all 103 pixels during the motion-tracking experiment. These signals are converted into a sparse Address-Event Representation (AER) format (Fig. 5b(ii)), commonly used in event-based cameras. In the AER output, blue dots indicate positive spikes (arrival of light), while red dots represent negative spikes (departure of light). Pixels without significant activity remain silent, ensuring data efficiency. By capturing and logging these spike events over time, together with the coordinates of corresponding pixels, the system reconstructs a temporal trace of the moving light spot across the sensor array. A dot-mapping video illustrating this process is provided in Supplementary Movie 5, with representative and all frames shown in Fig. 5b(iii) and Supplementary Fig. 19, respectively. Here, the yellow region marks the instantaneous light spot, while the purple trail indicates the cumulative trajectory formed by sequential events. To improve the accuracy, a simple neural network was employed to regress the car trajectory on the sphere (orange curve in Fig. 5b(iv)), with the algorithm details provided in Supplementary Methods. From the trace on the spherical device, the car trace on the ground can be further reconstructed (Fig. 5b(v)). Briefly, each ommatidium has a fixed pointing direction, from which the incident angle of light is inferred for each activated pixel. By extending these direction vectors, their intersections with the table surface yield the instantaneous positions of the light spot. Connecting these points and averaging with respect to angle reconstructs the motion path on the table. Given the height of the ASCE, this approach enables an accurate 3D-to-2D projection of the car's trajectory. As shown in Fig. 5b(vi), the reconstructed path closely matches the true trajectory, with a small mean relative error (MER) of 0.011.

To further validate this capability, we tilted the ASCE to mimic flight attitude changes during drone operation. The device was tilted by 40° and tested under the same motion-tracking setup. As expected, the responsive pixel region shifts with the illuminated area, yet the reconstructed trajectory remains closely aligned with the ground truth (Fig. 5c(i–iii) and Supplementary Figs. 20 and 21). This confirms that the event-driven, bioinspired compound eye can robustly track motion across an ultrawide field of view, even under dynamic orientations. The slight error increase is attributed to lower pixel density near the equator. These results highlight the ASCE's potential for real-world aerial vision tasks.

Further scaling of the pixel array and circuit integration will be essential to enable more advanced functionalities, and will require co-design of the device and read out integrated circuit (ROIC). In our device, the nanowire density is sufficient. The main limitation is electrode density/routing. Although standard lithography is challenging on a spherical surface, alternative approaches such as laser writing, printing, and transfer could increase top-electrode density, while the Al sphere can be patterned to improve the bottom-electrode array. At higher pixel densities, thinner/denser in-plane interconnects increase R and parasitic C, leading to larger RC delay, so 3D vertical integration is preferred. Besides, with the scalability of pixels, full parallel reading with multiple SMUs becomes less feasible, and the asynchronous event-camera ROICs are promising to improve integration without sacrificing response speed.

Discussion:

The unique structural features of insects can serve as a rich source of inspiration for innovations in drone design and engineering. In this work, we focus on motion detection—a critical function in various biological activities such as prey capture and predator avoidance. To replicate key biological advantages such as low power consumption, minimal computational load, and low latency, we have designed and fabricated an artificial compound eye visual system with several distinctive features: i) Wide FoV. the system offers a wide FoV of approximately 294°, enabled by its spherical architecture, which arises from the conformal growth of nanowires and bottom Al2O3 layer on curved surface. The wide FoV enhances panoramic visual coverage and enabling early detection of moving targets. ii) Event nature photoresponse of pixels. The pixels are selectively response to temporal change of light. They exhibit motion sensitive response, where faster motion induces stronger and quicker electrical signals, enabling real-time, computation-free motion detection. 8 ns response time is achieved for the femtosecond laser stimuli. iii) Self-powered property. Their intrinsic photovoltaic behavior supports self-powered operation, making the system ideal for continuous, low-cost surveillance applications. Additionally, enhanced long-term stability is achieved through material encapsulation and the adoption of alternating current spiky operational modes, ensuring reliable performance over extended periods. Together, these features make the system highly suitable for deployment in lightweight, edge-computing platforms such as drones, autonomous robots, and mobile surveillance systems.

To demonstrate the application potential of our system, we have explored different level-of-use cases, including individual pixel-based edge extraction and motion detection, an end-to-end four-quadrant drone alarming system and a 103-pixel array-based car moving monitoring. While the demonstrated capabilities mark a significant advancement, the low pixel density remains a key limitation, constraining spatial resolution and hindering broader deployment. Overcoming this challenge will require collaborative progress in both device architecture and measurement infrastructure. Integration with a CMOS ROIC presents a promising path toward improving resolution and enabling real-time, high-throughput operation. Overall, this work offers a streamlined and scalable solution for high-performance, bioinspired vision, establishing a paradigm for autonomous, energy-efficient vision systems with broad potential in drones and robotics for surveillance and real-time motion tracking.

Methods:

Device fabrication

Fabrication of spherical artificial compound eye. A high-purity aluminum sphere (>99.7% purity) with a diameter of 2.54 cm was washed in ethanol by an ultrasonic cleaner. A 2 mm thick Al wire was sticked vertically to the sphere surface with silver paste as the electrode and protected with ultraviolet curing epoxy (NOA81). Then, it was electrochemically polished in $HClO_4$-ethanol solution (1:3) at 13 V for 3 min, and rinsed in DI water. The polished AAO was first anodized in H_3PO_4-glycol-H_2O (0.8:100:200) at 200 V for 10 h, and etched in CrO_3 (1.8%)-H_3PO_4 (6%)-H_2O solution at 100 °C for 30 min. After etching, the sample was 2nd anodized for another 1.5h for homogeneous AAO growth. The obtained AAO was immersed into 0.2 mol/L H_3PO_4 solution for barrier thinning. The sample was firstly applied to a gradually increasing voltage, with a step of 10 V. Once the voltage attained 190 V, the power supply was immediately changed to constant current mode at 24 mA. The process stopped when the voltage value decreased to 4 V. The barrier thinned region was put into $PbCl_2$ (1.3%)-sodium citrate (20%)-H_2O solution for Pb electrochemical deposition under increasing AC voltage to an amplitude of 4 V for 20 min. Subsequently, a container, containing both the sample and Methylammonium iodide (MAI) powder, was placed inside a tubular furnace for chemical vapor deposition (CVD) at 183°C in Argon atmosphere for 4 h. An array of circular ITO electrodes with a diameter of 2 mm and a thickness of 30 nm were sputtered. The copper pads on the FPCB corresponded one-to-one with the pixels in position. Then, one end of a short copper wire was soldered to a pad on the FPCB, and the other end was secured to an ITO electrode using conductive adhesive.

The black pinhole mask was fabricated using two hemispherical PDMS shells. The PDMS monomer and curing agent were thoroughly mixed at a weight ratio of 10:1, with extra 1 wt% carbon black powder. The homogeneous mixture was poured into a 3D-printed mold featuring a semi-spherical cavity with cylindrical supports. A spherical ball was used to compress the mixture, ensuring the formation of a concave inner surface conforming to the sample geometry. The assembly was degassed under vacuum and subsequently cured in an oven at 80°C for 6 hours. After demolding, all pinhole channels were cleared. A hemispherical lens (K9 glass, 2 mm diameter) was attached over each pinhole using UV-curable adhesive. Finally, the two PDMS masks were aligned and fixed onto the upper and lower surfaces of the sample.

Preparation of high fill factor samples. The 2nd anodized AAO samples were immersed into 5% H_3PO_4 solution heated to 52 °C for 5 min, 10 min and 20 min respectively. The longer treatment time, the larger the pore size of the samples. The 2nd etched samples were re-anodized at 200 V for another 5 min to grow the barrier layer to enough thickness. The remaining steps were consistent with the preparation of the previous unetched samples.

Preparation of freestanding samples. The planar sample was fabricated onto a 20 mm × 20 mm × 0.2 mm Al sheet with the same process. A grid pattern was carefully scratched onto the back side of the sample using a knife. Then the sample was immersed into 1 M NaOH solution to remove the back AAO layer. The exposed Al substrate was further etched by 0.5 M $CuCl_2$ solution. The back AAO barrier layer was ion milled at 58 mA beam current with a tilt angle of 45° for 1 h. The sample and MAI powder were put into the tubular furnace for 10 min CVD regrowth. The gold electrodes were evaporated onto both sides of the pristine and ion-milled samples.

Photodetection characterization of individual pixel

Photodetection measurement. The photodetection measurement of the perovskite nanowire array devices utilized three different light modulation methods: chopper, DMD, and femtosecond laser. The chopper (Stanford Research Systems, Inc.) was inserted between the sample and a white LED light. When the chopper blade rotated, the current generated by the sample was collected by NI 4135 SMU (National Instruments Corp.) with the sampling rate of 10 kHz. The DMD (Texas Instruments, Inc.) setup used 470 nm LED light with a collimator. The illumination states were controlled by a home-made program. And the electric signal was measured at 100 kHz sampling rate. The specific detectivity (D*) under this condition was calculated by the formula of

$$D^* = R \cdot \sqrt{A} \Big/ \sqrt{2eI_{\mathrm{dark}}} \quad (1)$$

where R is the responsivity, A is the pixel area, I_{dark} is the dark current, and e is the elementary charge. The ultrafast response testing was performed using 515 nm femtosecond laser (Axinite GR, Bellin Laser Co., Ltd.) featuring a pulse width of 300 fs. The light pulse frequency was 100 kHz and the laser output power was 2 W. The single pulse energy was 20 µJ. The laser beam was TM00 mode (M2 < 1.3), with a diameter of 2.5 mm, larger than the measured pixel. The sample output was tested by Tektronix oscilloscope at 1 GHz sampling rate.

Photoresponse stability test. The continuous stability test was achieved by chopper and NI 4135 SMU. The chopping frequency was set to 100 Hz, and the SMU sampling rate was 10 kHz. The SMU was controlled to measure the signal for 10 s and waited for the data I/O operation. This process was repeated uninterruptedly for 14 days.

Edge extraction based on individual pixel. The optical experiment setup was mainly composed of an LED, a collimator, a digital micromirror device (DMD), and a mirror, as shown in Fig. 2d(i). The parallel 470 nm light from LED light source and the matching collimator (Daheng New Epoch Technology, Inc.) covered the whole mirror region of DMD. This DMD consisted of 1024 micromirror columns by 768 micromirror rows. Each micromirror corresponded to a single pixel owning two states- on and off. And the whole area was controlled by a computer program by inputting the same dimension (1024 × 768) of black-white binary images. The white pixels made the corresponding micromirrors on while black pixels in the image turned them off. Finally, the patterned parallel light was projected onto the sample surface after passing a mirror. To embody the characteristics of edge and motion detection, our sample pixel was fixed on the optical table and a series of dynamic patterns were played onto it.

Specifically, we flattened 86 × 86-pixel Mickey Mouse picture into a one-dimensional vector, and replace the 1/0 values with pure white/black images respectively. Playing this series of images with 200 Hz frame frequency was equivalent to the original picture moving horizontally pixel by pixel over the sample. When two adjacent images were different, a current pulse was generated- black to white transfer generated a positive peak while white to black lead to a negative one.

We collected the I-t curves at 10 kHz sampling rate. From every 50 (10 kHz/200 Hz) current data, we selected the one with the absolute maximum value to represent the pixel response, and then the obtained current array was reshaped back to 86 × 86. From the result, we could see the boundary of the image was extracted (Fig. 2d(ii)), and the left edge was red (negative) while the right edge was blue (positive). Adding a transpose process before the image array flattening, the image scan direction was transferred from horizontal to vertical. In the same way, we scanned the 70 × 70 pixels solid circle pattern in horizontal direction, and the 400 × 400 pixels SJTU logo in both two directions (Supplementary Fig. 5). Each result obtained the only one direction boundary information. We combined these two together by selecting pixel with the larger absolute value, and this reunion result showed the edge details clearly.

Motion detection based on individual pixel. For motion detection, we input a sequence of ten 124 × 124 pixels binary images, which was represented by an array with the dimension of (124, 124, 10). We overlapped them together by moving the 3rd axis to the 1st place, generating a new array of (10, 124, 124), and then flattened it to one-dimensional vector, followed by the same test process. In this way, we measured the difference of every single pixel between each two consecutive images. By reversing the previous array operation—reshaping and axis moving—we reconstructed the motion part in the sequence, as shown in Supplementary Movie 1. Blue color (positive current) indicated newly appearing pixels in the subsequent image, and red color (negative current) indicated regions that vanished from the previous image.

Silvaco Technology Computer-Aided Design simulation

Device physics simulations were performed using Silvaco Atlas (version 5.19.20.R) to investigate the optoelectronic behavior of a planar perovskite photosensor, designed to emulate the response of the experimental nanowire-based device. The simulated device consisted of a multilayer stack with the following structure: $Al/Al_2O_3/MAPbI_3/PCBM/ITO$, where Al and ITO served as the bottom and top electrodes, respectively. The Al_2O_3 layer thickness was set to ~5 nm based on experimental measurements. The physical and electronic parameters of all materials used in this simulation were extracted from literatures65,66 and were further summarized in Supplementary Fig. 9. Simulations were conducted under illumination with a standard AM 1.5G light source at an intensity of 100 mW/cm^2. The rising and falling edges of the light pulses were varied to simulate different optical pulse profiles. The simulation outputs included current-time (I-t) characteristics, as well as the spatial distributions of electron and hole concentrations under both dark and illuminated conditions, enabling analysis of charge transport dynamics and photogeneration.

Drone alarming system based on artificial spherical compound eyes

Circuits design. The FPCB circuit consisted of amplifier (AD825), inverter (74HC04), RS flip-flop latch (SN74LS279) and MOSFET (IRF540N), and resistors, diodes and capacitors. The flexible PCB was made in PET with a thickness of 125 μm. The electronic components were mounted onto PCB with solder paste as shown in Supplementary Fig. 16a. The circuit was powered by two 6V batteries. Upon illumination, a positive input pulse set the Q state of the RS flip-flop latch to low, initiating a discharge pathway through the upper branch of the circuit (Supplementary Fig. 16c). This led to a reduction in the voltage across the capacitor, resulting in a high output voltage at the final transistor stage. Conversely, a negative input pulse reset the output to a low voltage state, while a zero input maintained the current logic state. When the laser beam struck the device, a positive pulse was generated, triggering the drone's evasive maneuver. The drone continued to move away from the beam until the system detected a return to low voltage, indicating the absence of the stimulus. To optimize both temporal responsiveness and operational safety, the system employed decoupled charging and discharging pathways. This resulted in an asymmetric output profile characterized by a fast-rising edge for immediate activation and a slow-falling edge that prolonged the response duration. The extended decay acted as a safety buffer, preventing premature termination of the escape behavior. We used the signal generator to simulate the peak output of our perovskite nanowire dynamic vision sensor. Tektronix oscilloscope measured the waveforms at input and corresponding output terminals of conversion PCB, as shown in Supplementary Fig. 16b. We put another oscilloscope probe at the output pin of the amplifier to show the output in middle, and compared all the waveforms in Fig. 4c(ii).

Drone alarming and control system. The drone alarming and control system was mainly composed of the artificial compound eye, custom-designed circuits, Raspberry Pi and Pixhawk flight controller. Four pixels of our artificial compound eye distributed on the equator at 90° intervals were connected to the input terminals of the customed-designed PCB, and the common bottom electrode was connected to the ground terminal, as shown in Fig. 4b. The four PCB output terminals and the ground were connected to five pins of the Raspberry Pi, so that the transferred voltage signals could be collected by a python program. Once the hazardous light source illuminated one pixel, the corresponding FPCB output terminal generated a high-level voltage signal. The Raspberry Pi read it and then sent a message to Pixhawk to control the drone moving towards the opposite direction of the alarming signal. When the danger had passed for a while, the low-level voltage of FPCB output controlled the drone to stop moving, as shown by Supplementary Movie 3.

High-speed car motion tracking based on artificial spherical compound eyes

Experimental setup. The bio-inspired compound eye device was positioned above the desktop and secured using a clamp with a magic arm. By adjusting the angle of the magic arm, the device was able be oriented into different attitudes. Via FFC cables and an adapter, the ommatidia pixels and the common electrode were connected to five 24-channel PXIe-4163 SMUs (National Instruments Corp.) (Supplementary Fig. 18). A small 520 nm wavelength laser source was fixed on top of a remote-controlled car. The car was driven rapidly around the compound eye device on the desktop. As the laser spot continuously swept across the pixels on the device, event signals were generated.

Data acquisition. A home-made Python program was used to control all the 103 SMU channels to simultaneously read the current signals of individual pixels, producing 103 I-t curves. The sampling rate was set as 10 kHz under 0 voltage bias. Afterwards, the I-t data were reformatted into AER (Address-event representation) format, where blue points indicated positive current peaks and red ones indicated negative current peaks. The output events of the pixels at different time were plotted on a 3D sphere according to the coordinate of pixels, forming the trace on the spherical eye device.

Trajectory reconstruction. The trajectory equation on the spherical was obtained through fitting using a neural network algorithm, which comprised an input layer, three 64-dimensional hidden layers, and an output layer. Each layer was fully connected, and the

ReLU activation function was employed between layers. The input consisted of the normalized 3D Cartesian coordinates (x, y, z) of the response pixel points on the unit sphere. And the output predicted the normal vector $\mathbf{n} = (n_x, n_y, n_z)$ of the plane containing the trajectory and the angle θ formed between the line connecting the sphere center to the trajectory and the normal vector. From these outputs, the direction and radius of the trajectory were able to be derived. The loss function was composed of three parts: planar consistency loss, spherical distance loss and regularization terms.
Planar consistency loss ensured all points laying approximately in the same plane:

$$\mathcal{L}_{\text{planar}} = \text{Var}(P \cdot \mathbf{n}) \tag{2}$$

where $P \in \mathbb{R}^{(3\times\mathrm{N})}$ was the matrix of input points, and $\text{Var}(\cdot)$ computed variance.
Spherical distance loss minimized the angular distance between points and the fitted trajectory:

$$d_i = \left|\arccos\left(\frac{\mathbf{p}_i \cdot \mathbf{n}}{||\mathbf{p}_i||}\right) - \theta\right| \tag{3}$$

$$\mathcal{L}_{\text{spherical}} = \frac{1}{N}\sum_{i=1}^{N} d_i^2 \tag{4}$$

Regularization terms:

$$\mathcal{L}_{\text{reg}} = \lambda_1 |||\mathbf{n}|| - 1| + \lambda_2 \max(0, |\cos\theta| - 0.99)^2 \tag{5}$$

where $\lambda_1 = \lambda_2 = 0.01$.
The total loss was a weighted combination:

$$\mathcal{L}_{\text{total}} = \mathcal{L}_{\text{planar}} + \mathcal{L}_{\text{spherical}} + \mathcal{L}_{\text{reg}} \tag{6}$$

The orientation of the sphere was adjusted according to the computed normal vector of the trajectory, ensuring that the normal vector remained perpendicular to the table plane. Based on the FoV of a single pixel, rays were extended from the center point to the boundaries of the trajectory until they intersected with the table plane. The median curve of the resulting intersection annulus was defined as the car's motion trajectory (blue line in Fig. 5b(v)). The deviation of the trajectory was then quantified by calculating the difference, across the full 2π range, between the distance from this curve to the origin and the actual radius of the car's path (Fig. 5b(vi)). The mean relative error (MRE) was calculated by:

$$\text{MRE} = \frac{1}{n}\sum_{i=1}^{n} \left|\frac{y_i - \hat{y}_i}{y_i}\right| \tag{7}$$

Data Availability:

All the data required to assess the conclusions of the article are available via Figshare at https://doi.org/10.6084/m9.figshare.32050119 (Ref. 67).

Code Availability:

The code for fitting the car trajectory on the sphere is available in the Zenodo repository at https://doi.org/10.5281/zenodo.20094340 (Ref. 68).

References:

1. Meier, L., Tanskanen, P., Fraundorfer, F. & Pollefeys, M. PIXHAWK: A system for autonomous flight using onboard computer vision. in 2011 IEEE International Conference on Robotics and Automation 2992–2997 (IEEE, 2011).
2. Wang, Y., Ji, J., Wang, Q., Xu, C., & Gao, F. Autonomous flights in dynamic environments with onboard vision. In 2021 IEEE/RSJ International Conference on Intelligent Robots and Systems (IROS) 1966–1973 (IEEE, 2021).
3. Srinivasan, M. V., Poteser, M. & Kral, K. Motion detection in insect orientation and navigation. Vision Res. 39, 2749–2766 (1999).
4. Land, M. F. Visual acuity in insects. Annu. Rev. Entomol. 42, 147–177 (1997).
5. Dai, B. et al. Biomimetic apposition compound eye fabricated using microfluidic-assisted 3D printing. Nat. Commun. 12, 6458 (2021).
6. Hu, Z.-Y. et al. Miniature optoelectronic compound eye camera. Nat. Commun. 13, 5634 (2022).
7. Jiang, H. et al. Optical fibre based artificial compound eyes for direct static imaging and ultrafast motion detection. Light Sci. Appl. 13, 256 (2024).
8. Xie, Y. et al. First demonstration of 2.5D out-of-plane-based hybrid stacked super-bionic compound eye CMOS chip with broadband (300–1600 nm) and wide-angle

(170°) photodetection. in 2024 IEEE International Electron Devices Meeting (IEDM) 1–4 (IEEE, 2024).

9. Chen, S. et al. Optical aberrations correction in postprocessing using imaging simulation. ACM Trans. Graph. 40, 1–15 (2021).
10. Li, A. et al. Computational method for correcting complex optical distortion based on FOV division. Appl. Opt. 54, 2441 (2015).
11. Sahin, F. E. & Tanguay, A. R. Distortion optimization for wide-angle computational cameras. Opt. Express 26, 5478 (2018).
12. Kim, M. et al. An aquatic-vision-inspired camera based on a monocentric lens and a silicon nanorod photodiode array. Nat. Electron. 3, 546–553 (2020).
13. Choi, C. et al. Anti-distortion bioinspired camera with an inhomogeneous photo-pixel array. Nat. Commun. 15, 6021 (2024).
14. Floreano, D. et al. Miniature curved artificial compound eyes. Proc. Natl. Acad. Sci. 110, 9267–9272 (2013).
15. Song, Y. M. et al. Digital cameras with designs inspired by the arthropod eye. Nature 497, 95–99 (2013).
16. Gu, L. et al. A biomimetic eye with a hemispherical perovskite nanowire array retina. Nature 581, 278–282 (2020).
17. Zhou, Y. et al. An ultrawide field-of-view pinhole compound eye using hemispherical nanowire array for robot vision. Sci. Robot. 9, eadi8666 (2024).
18. Liu, S. et al. Conformability of flexible sheets on spherical surfaces. Sci. Adv. 9, eadf2709 (2023).

19. Rao, Z. et al. Curvy, shape-adaptive imagers based on printed optoelectronic pixels with a kirigami design. Nat. Electron. 4, 513–521 (2021).
20. De Croon, G. C. H. E. et al. Accommodating unobservability to control flight attitude with optic flow. Nature 610, 485–490 (2022).
21. Srinivasan, M. V. & Lehrer, M. Temporal acuity of honeybee vision: behavioural studies using moving stimuli. J. Comp. Physiol. A 155, 297–312 (1984).
22. Adrian, E. D. The electric response of the human eye. J. Physiol. 104, 84–104 (1945).
23. Zhu, L. et al. Ultra-compact on-chip camera based on optoelectronic compound eyes with nonuniform ommatidia. Int. J. Extreme Manuf. 7, 015502 (2025).
24. Delbruck, T. & Lichtsteiner, P. Fast sensory motor control based on event-based hybrid neuromorphic-procedural system. 2007 IEEE International Symposium on Circuits System (ISCAS) 845–848 (IEEE, 2007).
25. Amir, A. et al. A low power, fully event-based gesture recognition system. in 2017 IEEE Conference on Computer Vision and Pattern Recognition (CVPR) 7388–7397 (IEEE, 2017).
26. Liu, S.-C., Rueckauer, B., Ceolini, E., Huber, A. & Delbruck, T. Event-driven sensing for efficient perception: vision and audition algorithms. IEEE Signal Process. Mag. 36, 29–37 (2019).
27. Falanga, D., Kleber, K. & Scaramuzza, D. Dynamic obstacle avoidance for quadrotors with event cameras. Sci. Robot. 5, eaaz9712 (2020).
28. He, B. et al. Microsaccade-inspired event camera for robotics. Sci. Robot. 9, eadj8124 (2024).

29. Gehrig, D. & Scaramuzza, D. Low-latency automotive vision with event cameras. Nature 629, 1034–1040 (2024).
30. Lichtsteiner, P., Posch, C. & Delbruck, T. A 128×128 120 dB 15 μs latency asynchronous temporal contrast vision sensor. IEEE J Solid-State Circuits 43, 566-576 (2008).
31. Brandli, C., Berner, R., Minhao Yang, Liu, S. C. & Delbruck, T. A 240×180 130 dB 3 μs latency global shutter spatiotemporal vision sensor. IEEE J. Solid-State Circuits 49, 2333–2341 (2014).
32. Gallego, G. et al. Event-based vision: a survey. IEEE Trans. Pattern Anal. Mach. Intell. 44, 154–180 (2022).
33. Fernández-Peramo, P., Leñero-Bardallo, J. A. & Rodríguez-Vázquez, Á. A photovoltaic dynamic vision sensor. IEEE J. Solid-State Circuits 1–11 (2025).
34. Zhou, Y. et al. Computational event-driven vision sensors for in-sensor spiking neural networks. Nat. Electron. 6, 870-878 (2023).
35. Feng, G. et al. In-memory ferroelectric differentiator. Nat. Commun. 16, 3027 (2025).
36. Borst, A., Haag, J. & Mauss, A. S. How fly neurons compute the direction of visual motion. J. Comp. Physiol. A 206, 109–124 (2020).
37. Song, H. et al. Fully memristive elementary motion detectors for a maneuver prediction. Adv. Mater. 36, 2309708 (2024).
38. Yonehara, K. & Roska, B. Motion detection: neuronal circuit meets theory. Cell 154, 1188–1189 (2013).
39. Dou, L. et al. Solution-processed hybrid perovskite photodetectors with high detectivity. Nat. Commun. 5, 5404 (2014).

40. Lin, Q., Armin, A., Lyons, D. M., Burn, P. L. & Meredith, P. Low noise, IR-blind organohalide perovskite photodiodes for visible light detection and imaging. Adv. Mater. 27, 2060–2064 (2015).
41. Zeng, J. et al. Space-confined growth of CsPbBr3 film achieving photodetectors with high performance in all figures of merit. Adv. Funct. Mater. 28, 1804394 (2018).
42. Blanche, P. A., LaComb, L., Wang, Y. & Wu, M. Diffraction-based optical switching with MEMS. Appl. Sci. 7, 411 (2017).
43. Posch, C., Matolin, D. & Wohlgenannt, R. A QVGA 143 dB dynamic range frame-free PWM image sensor with lossless pixel-level video compression and time-domain CDS. IEEE J. Solid-State Circuits 46, 259–275 (2011).
44. Posch, C., Matolin, D. & Wohlgenannt, R. A QVGA 143dB dynamic range asynchronous address-event PWM dynamic image sensor with lossless pixel-level video compression. in 2010 IEEE International Solid-State Circuits Conference (ISSCC) 400–401 (IEEE, 2010).
45. Finateu, T. et al. A 1280×720 back-illuminated stacked temporal contrast event-based vision sensor with 4.86µm pixels, 1.066GEPS readout, programmable event-rate controller and compressive data-formatting pipeline. in 2020 IEEE International Solid- State Circuits Conference (ISSCC) 112–114 (IEEE, 2020).
46. Son, B. et al. A 640×480 dynamic vision sensor with a 9µm pixel and 300Meps address-event representation. in 2017 IEEE International Solid-State Circuits Conference (ISSCC) 66–67 (IEEE, 2017).

47. Rebecq, H., Ranftl, R., Koltun, V. & Scaramuzza, D. High speed and high dynamic range video with an event camera. IEEE Trans. Pattern Anal. Mach. Intell. 43, 1964–1980 (2019).
48. Suh, Y. et al. A 1280x960 dynamic vision sensor with a 4.95-μm pixel pitch and motion artifact minimization. in 2020 IEEE international symposium on circuits and systems (ISCAS) 1–5 (IEEE, 2020).
49. Guo, M., Huang, J. & Chen, S. Live demonstration: A 768×640 pixels 200Meps dynamic vision sensor. in 2017 IEEE International Symposium on Circuits and Systems (ISCAS) 1–1 (IEEE, 2017).
50. Chen, S. & Guo, M. Live demonstration: CeleX-V: a 1M pixel multi-mode event-based sensor. in 2019 IEEE/CVF Conference on Computer Vision and Pattern Recognition Workshops (CVPRW) 1682–1683 (IEEE, 2019).
51. Gu, L. et al. 3D arrays of 1024-pixel image sensors based on lead halide perovskite nanowires. Adv. Mater. 28, 9713–9721 (2016).
52. Zai, H., Ma, Y., Chen, Q. & Zhou, H. Ion migration in halide perovskite solar cells: Mechanism, characterization, impact and suppression. J. Energy Chem. 63, 528–549 (2021).
53. Krishnaiah, M. et al. Physically detachable and operationally stable Cs2SnI6 photodetector arrays integrated with μ-LEDs for broadband flexible optical systems. Adv. Mater. 34, 2109673 (2022).
54. Ye, Q. et al. High-performance hierarchical O-SnS/I-ZnIn2S4 photodetectors by leveraging the synergy of optical regulation and band tailoring. Mater. Horiz. 9, 2364–2375 (2022).

55. Chen, H.-W. et al. A switchable high-sensitivity photodetecting and photovoltaic device with perovskite absorber. J. Phys. Chem. Lett. 6, 1773–1779 (2015).

56. Cao, F., Tian, W., Meng, L., Wang, M. & Li, L. Ultrahigh-performance flexible and self-powered photodetectors with ferroelectric P(VDF-TrFE)/perovskite bulk heterojunction. Adv. Funct. Mater. 29, 1808415 (2019).

57. Shi, B. et al. Split-ring structured all-inorganic perovskite photodetector arrays for masterly internet of things. Nano-Micro Lett. 15, 3 (2023).

58. Zhao, T. et al. Neuromorphic transistors integrating photo-sensor, optical memory and visual synapses for artificial vision application. Adv. Mater. 37, 2419208 (2025).

59. Choi, C. et al. Curved neuromorphic image sensor array using a MoS2-organic heterostructure inspired by the human visual recognition system. Nat. Commun. 11, 5934 (2020).

60. Li, G. et al. Photo-induced non-volatile VO2 phase transition for neuromorphic ultraviolet sensors. Nat. Commun. 13, 1729 (2022).

61. Zhang, Z. et al. In-sensor reservoir computing system for latent fingerprint recognition with deep ultraviolet photo-synapses and memristor array. Nat. Commun. 13, 6590 (2022).

62. Sutherland, B. R. et al. Sensitive, Fast, and Stable Perovskite Photodetectors Exploiting Interface Engineering. ACS Photonics 2, 1117–1123 (2015).

63. Tillyard, R. J., “The nervous system” in The Biology of Dragonflies:(Odonata or Paraneuroptera) (CUP Archive, 1917).

64. Simmons, P., The neuronal control of dragonfly flight: I. Anatomy. J. Exp. Biol. 71, 123–140 (1977).

65. Du, H. J., Wang, W. C. & Gu, Y. F. Simulation design of P-I-N-type all-perovskite solar cells with high efficiency. Chin. Phys. B. 26, 028803 (2017).

66. Eli, D. et al. Simulation and optimization of lead-based perovskite solar cells with cuprous oxide as a P-type inorganic layer. J. Niger. Soc. Phys. Sci., 72–81 (2024).

67. Wei, R. et al. A Self-powered Spherical Compound Eye with 8 ns-motion Response for Source-constrained Drones. Figshare https://doi.org/10.6084/m9.figshare.32050119 (2026).

68. Wei, R. et al. A Self-powered Spherical Compound Eye with 8 ns-motion Response for Source-constrained Drones. Zenodo https://doi.org/10.5281/zenodo.20094340 (2026).

Acknowledgments:

The authors acknowledge the company of Jujiao Optoelectronics Technology Co., Ltd. (JUOPT) for their support on DMD systems.

Funding:

L.G. discloses support for the research of this work from STI 2030—Major Projects (grant no. 2022ZD0210000) and National Science Foundation China (grant no. 62274110). B.T. discloses support for publication of this work from National Key Research and Development Program of China (grant no. 2024YFA1410700) and National Natural Science Foundation of China (grant no. T2222025, 62174053). The other authors declare no relevant funding.

Author Contributions Statement:

W.R., L.G., X.W. and Z.F. conceived the project. W.R., J.T., X.Z., D.N., L.W., Z.Y., B.T., J.C. and L.G. developed the methodology. W.R., X.Z., L.X., Y.Z., B.S., Q.M., Y.S., Z.H. conducted the experiments. W.R., J.T., X.Z., Q.C., B.S., Q.M. and L.G. were responsible for visualization. W.R. wrote the original draft, while L.X., Q.C., B.T. and L.G. reviewed and edited the manuscript.

Competing Interests Statement:

The authors declare no competing interests.

Figure Legends:

Fig. 1 | Overall illustration of artificial and natural compound eyes. a, Schematic comparison of the natural and artificial compound eyes. (i) The schematic of a dragonfly catching prey. (ii) The schematic of natural compound eye for efficient motion capture through elementary motion detectors. (iii) The architecture of artificial spherical compound eye for local motion estimation. b, A proposed application scenario of the artificial compound eye. (i) The photo of an artificial compound eye device with nanowire arrays (inset SEM image). (ii) The scenario of traffic flow monitoring using the artificial compound eye device and (iii) its output.

Fig. 2 | Photodetection characterization of the artificial spherical compound eye devices. a, The photograph of an artificial spherical compound eye mounted on a printed circuit board for testing. b, Field of View characterization of the artificial compound eye device. The peak photocurrent generated from optical pulses with different incident angles: along (i) the vertical direction (indicated by the blue line in Fig. 2a) and (ii) the horizontal equator direction (indicated by red line in Fig. 2a). c, Photodetection characterization of an individual pixel under 0 V bias. (i) A typical I-t curve. (ii) I-t characteristics tested under chopped illumination with different power densities (0.19–30.92 mW/cm2) at fixed frequency (100 Hz). (iii) I-t characteristics tested under chopped pulses at different chopper frequencies (10–400 Hz) with fixed light intensity (30 mW/cm2). (iv) I-t characteristics tested under digital micromirror device (DMD)-generated optical pulses at different frequencies (1–10 kHz) under fixed light intensity (9.27 mW/cm2). (v) Peak current and response time analysis with different light intensities (945 nW/cm2–9.27 mW/cm2) at fixed frequency (DMD generated pulses). (vi) V-t characteristics under femtosecond laser pulses (532 nm) illumination at 100 kHz. d, Single-pixel imaging demonstration. (i) Schematic of experiment setup based on DMD scanning. (ii) Edge extraction and (iii) motion detection.

Fig. 3 | Mechanism exploration of pixels in the artificial spherical compound eye. a, Schematic of device structure. (i) Structure schematic of a complete artificial spherical compound eye and (ii) a detailed single nanowire-based sensor. (iii) Technology Computer-Aided Design simulation results of hole distribution during photoresponse for devices with and without bottom Al2O3 layer. b, Experimental validation of the above mechanism from photoresponse of devices (i) with and (ii) without bottom Al2O3 layer. c, Ion migration suppression from the bottom Al_2O_3 layer. (i) The schematic and (ii) experimental results. The I-t curve is measured under continuous switching optical pulses (100 Hz chopped illumination, 30 mW/cm²), exhibiting high reproducibility with 108 cycles. d, Technology Computer-Aided Design simulation revealing mechanism of motion sensitive nature. The device is stimulated by fast (rising time: 0.1 μs) and slow (rising time: 1 μs) optical pulses, respectively. (i) The simulated I-t curves and the contour of (ii) photogeneration rate and (iii) hole accumulation at the time of light finishing rising (indicated by the dash circles).

Fig. 4 | An end-to-end, four-quadrant drone emergency-alarming system. a, Schematic of analogy between dragonfly neural circuit and artificial compound eye-based drone system, achieving the similar emergency avoidance task. b, Back-view photograph of the four-quadrant sensors system mounted on the drone. c, Schematic demonstration of end-to-end connections between quadrant sensors and propellers. (i) Quadrant control schematic and (ii) response time analysis of the system, where the signal changes at different steps are measured by oscilloscope probes placed on the circuit board. d, Experimental demonstration in artificial compound eye-based control of drone motion direction to avoid hazardous signals. Ground-based experiments on the device capturing light signals from (i) right and (ii) bottom, respectively. The system controls the corresponding propellers rotating, showing a tendency to move leftwards and upwards to escape from the danger. (iii) In-flight demonstration of drone avoiding the light hazardous signal from left.

Fig. 5 | High-speed car motion tracking demonstration. a, Experiment scenario and measurement setup. The simultaneous data acquisition (DAQ) mimics the parallel data processing in insects, reducing the latency in circuits. b, The dynamic data process pipeline and reconstruction result of artificial compound eye with vertical attitude. (i) Measured I-t curves of all the pixels in artificial compound eye device. (ii) Reshaped address-event-representation format data from the original I-t curves. (iii) Four representative frames of pixel responses and trace recorded on the artificial compound eye. (iv) Fitted trajectory on artificial compound eye. (v) Projected trajectory on the table. (vi) Deviation analysis of constructed trajectory from the real trace. c, Trace reconstruction from artificial compound eye with tilted attitude (40°), emulating the condition of flight attitude changing. (i) Four representative frames of pixel responses and trace recorded on the artificial compound eye. (ii) Fitted trajectory on artificial compound eye and (iii) the projected trajectory on the table.

Editorial summary:

This work demonstrates a self-powered, event-nature artificial spherical compound eye that achieved ultrafast and panoramic motion sensing under 0 V, particularly suitable for resource-limited drones and robotics.

Peer review information: *Nature Communications* thanks Young Min Song, and the other, anonymous, reviewer(s) for their contribution to the peer review of this work. A peer review file is available.

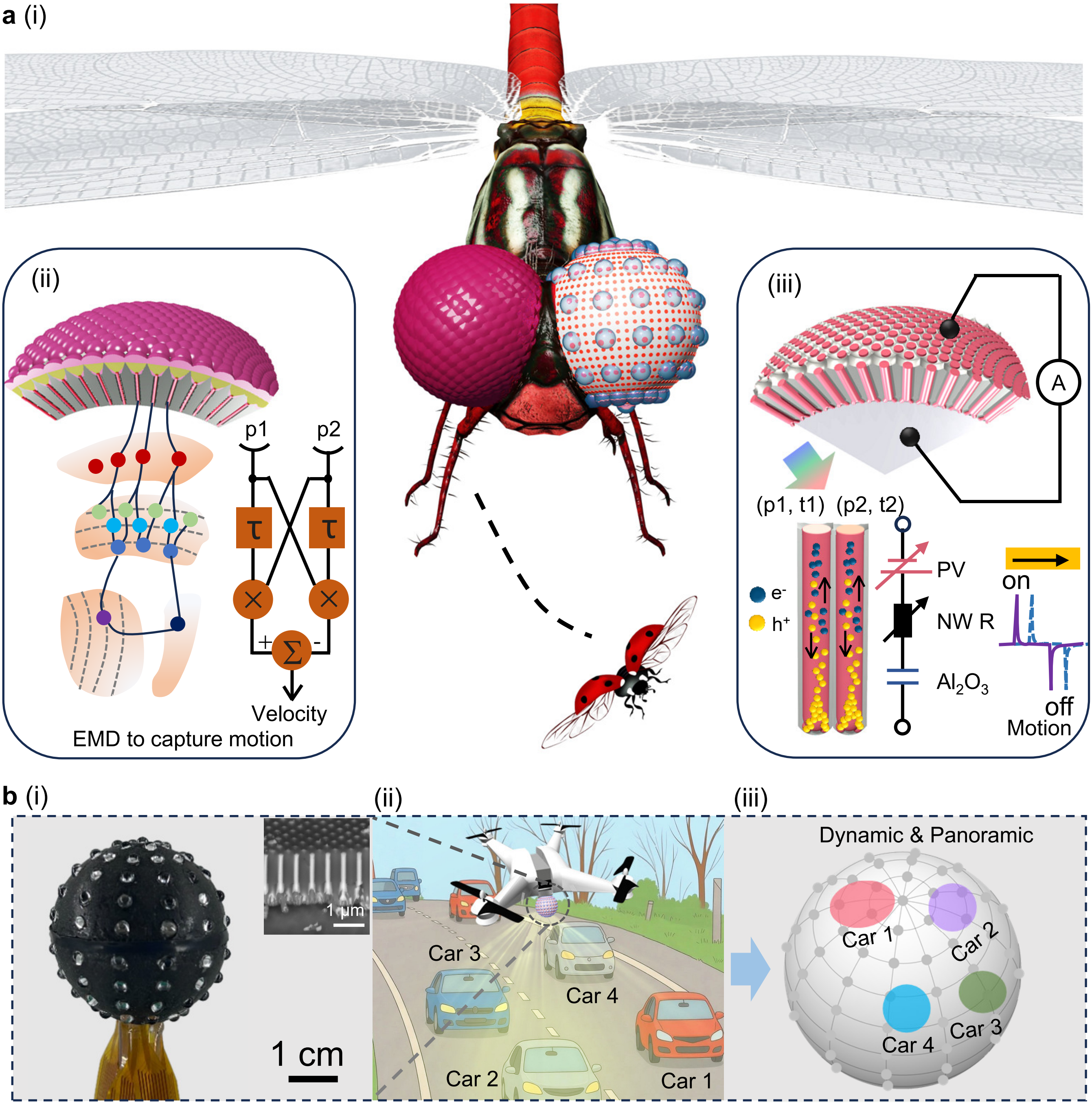
a (i)
(ii)
p1
p2
τ
τ
×
×
Σ
+
-
Velocity
EMD to capture motion
(iii)
A
(p1, t1) (p2, t2)
e-
h+
PV
NW R
Al2O3
on
off
Motion
b (i)
(ii)
(iii)
1 μm
1 cm
Car 3
Car 4
Car 2
Car 1
Dynamic & Panoramic
Car 1
Car 2
Car 4
Car 3

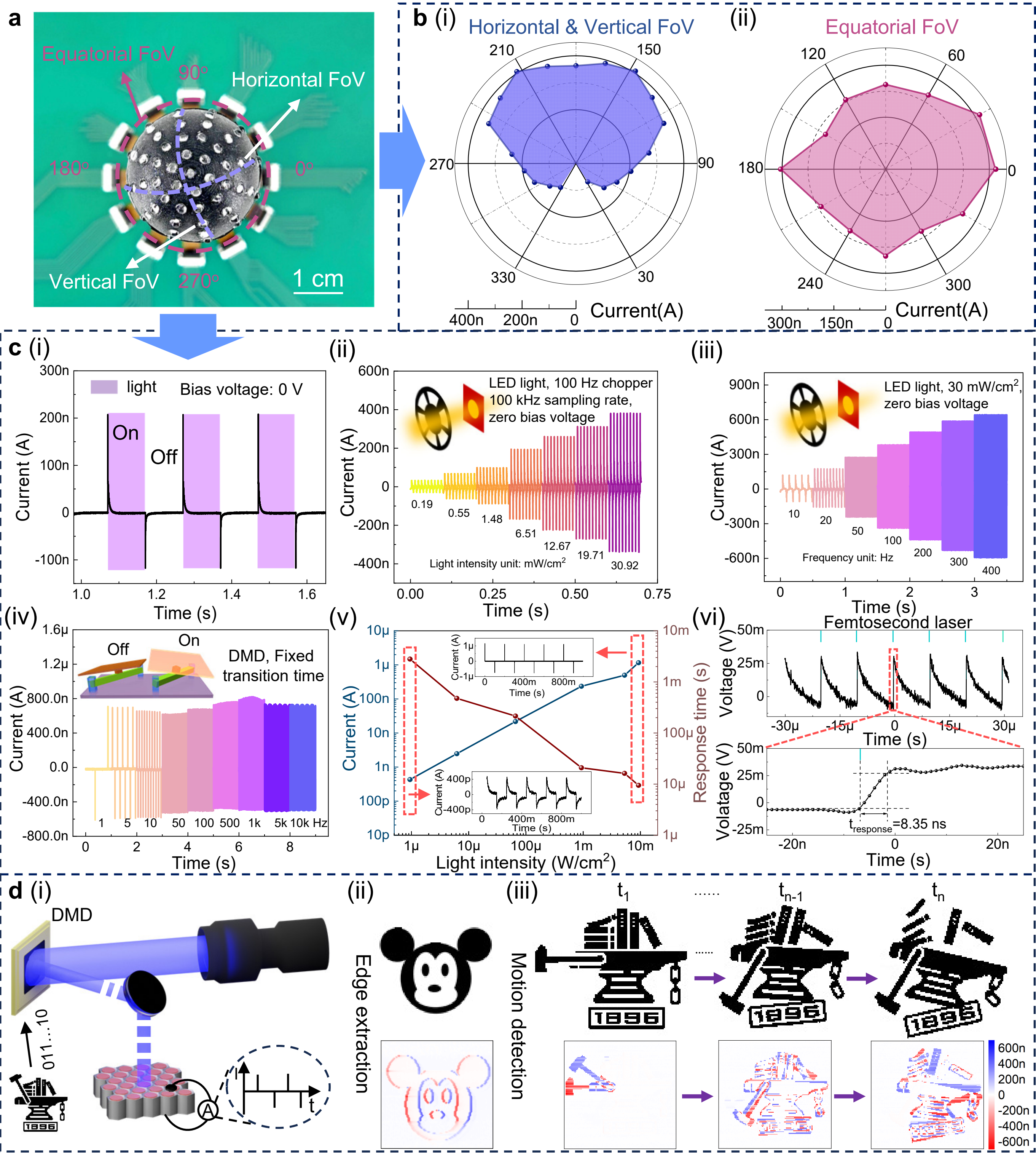
a
Equatorial FoV
90°
Horizontal FoV
180°
0°
Vertical FoV
270°
1 cm
b (i) Horizontal & Vertical FoV
(ii) Equatorial FoV
Current(A)
c (i) light Bias voltage: 0 V
On
Off
Current (A)
Time (s)
(ii) LED light, 100 Hz chopper 100 kHz sampling rate, zero bias voltage
Light intensity unit: mW/cm2
(iii) LED light, 30 mW/cm2, zero bias voltage
Frequency unit: Hz
(iv) DMD, Fixed transition time
Off
On
(v) Current (A)
Response time (s)
Light intensity (W/cm2)
(vi) Femtosecond laser
Voltage (V)
Volatage (V)
tresponse=8.35 ns
d (i) DMD
011...10
(ii) Edge extraction
(iii) Motion detection
t1
tn-1
tn
1896

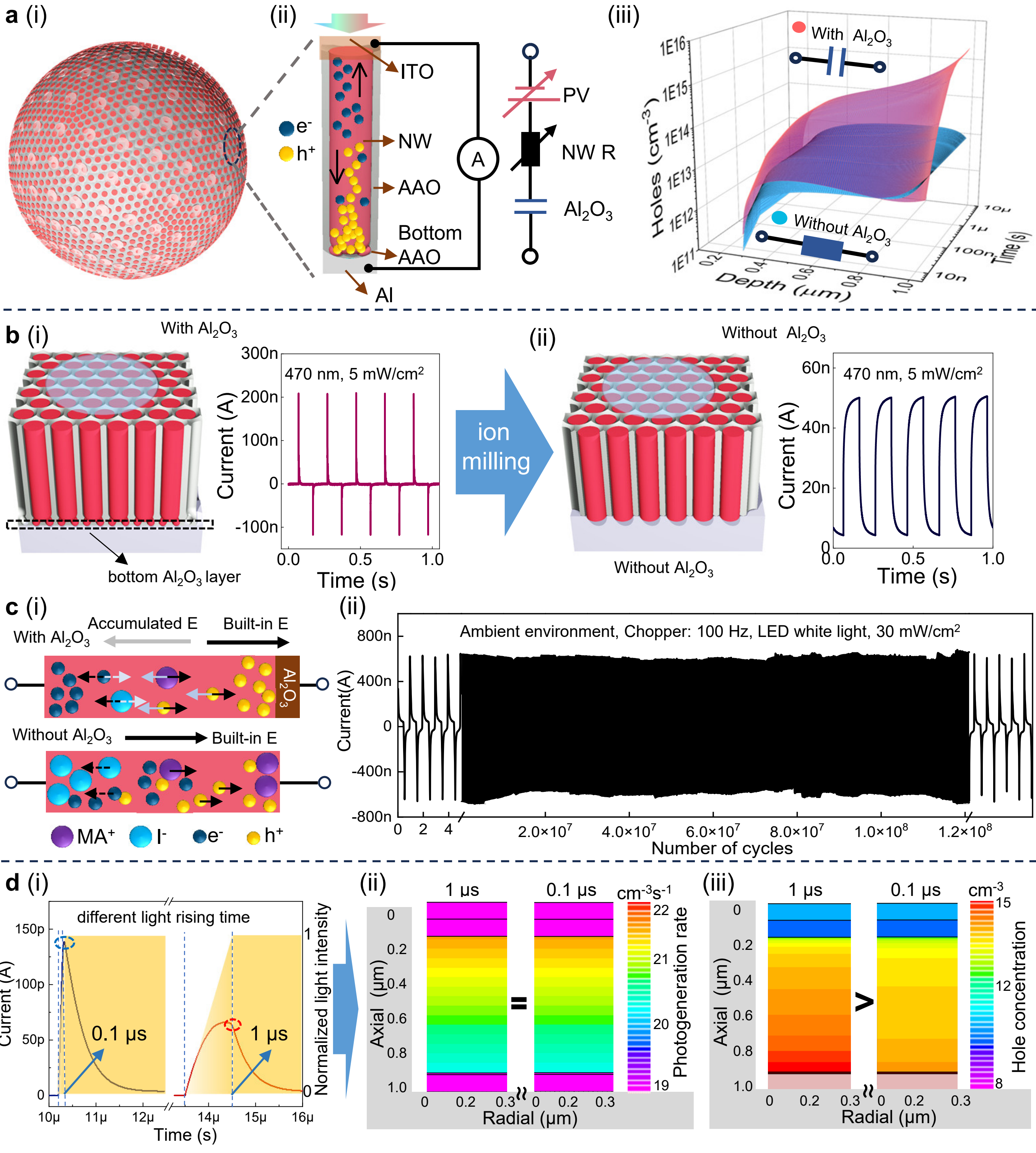
a (i) (ii) (iii)
e-
h+
ITO
NW
AAO
Bottom AAO
Al
A
PV
NW R
Al2O3
With Al2O3
Without Al2O3
Holes (cm-3)
Depth (μm)
Time (s)
b (i) With Al2O3
470 nm, 5 mW/cm2
Current (A)
Time (s)
bottom Al2O3 layer
ion milling
(ii) Without Al2O3
Without Al2O3
c (i)
Accumulated E
Built-in E
With Al2O3
Without Al2O3
MA+ I- e- h+
(ii)
Ambient environment, Chopper: 100 Hz, LED white light, 30 mW/cm2
Current(A)
Number of cycles
d (i)
different light rising time
0.1 μs
1 μs
Current (A)
Normalized light intensity
Time (s)
(ii) 1 μs 0.1 μs
cm-3s-1
Photogeneration rate
Axial (μm)
Radial (μm)
(iii) 1 μs 0.1 μs
cm-3
Hole concentration

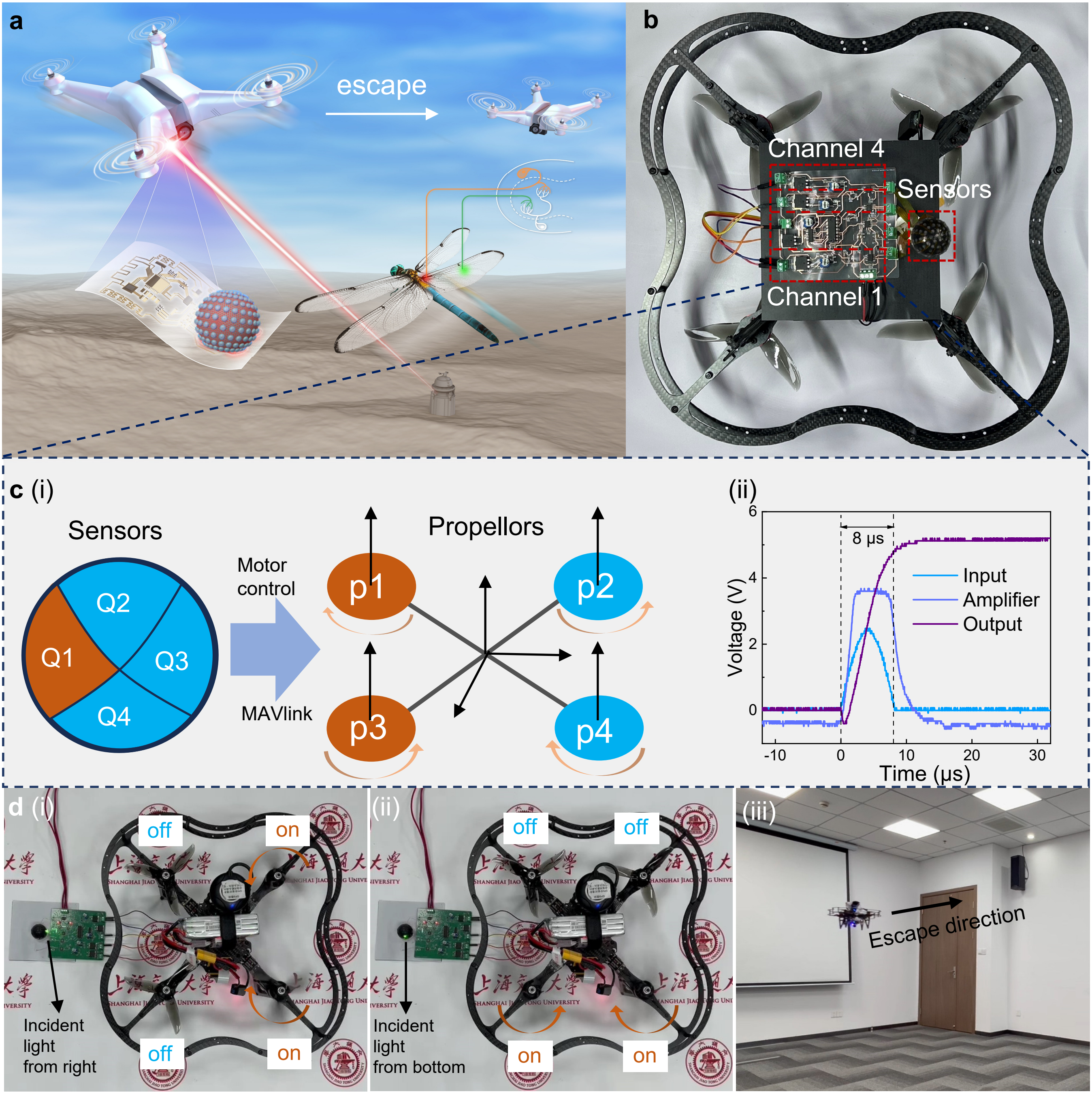
a
escape
b
Channel 4
Sensors
Channel 1
c (i)
Sensors
Q1
Q2
Q3
Q4
Motor control
MAVlink
Propellors
p1
p2
p3
p4
(ii)
8 μs
Input
Amplifier
Output
Voltage (V)
Time (μs)
d (i)
off
on
off
on
Incident light from right
(ii)
off
off
on
on
Incident light from bottom
(iii)
Escape direction

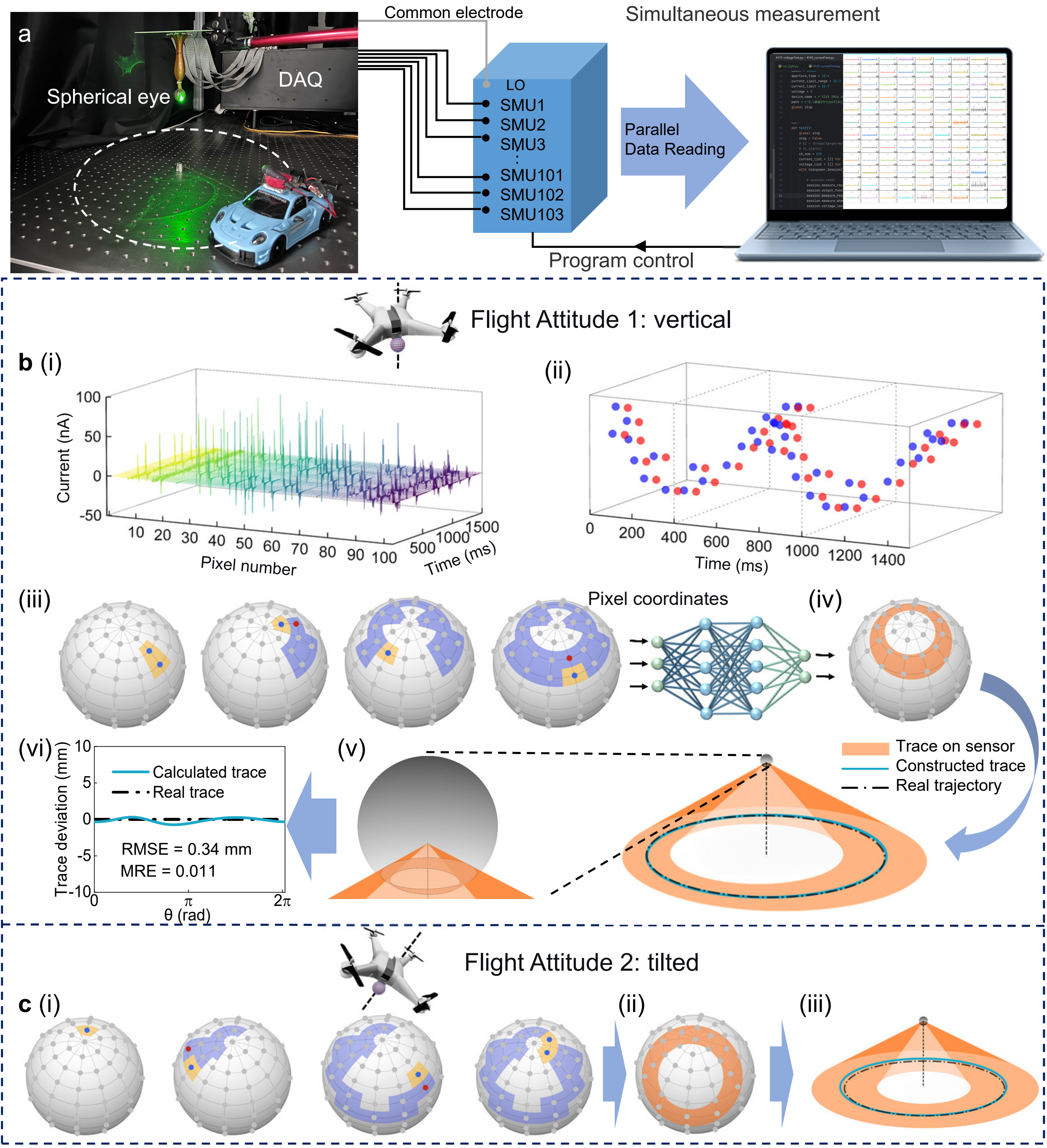
a
Spherical eye
DAQ
Common electrode
Simultaneous measurement
LO
SMU1
SMU2
SMU3
SMU101
SMU102
SMU103
Parallel
Data Reading
Program control
Flight Attitude 1: vertical
b (i)
Current (nA)
Pixel number
Time (ms)
(ii)
Time (ms)
(iii)
Pixel coordinates
(iv)
(v)
(vi)
Trace deviation (mm)
Calculated trace
Real trace
RMSE = 0.34 mm
MRE = 0.011
θ (rad)
Trace on sensor
Constructed trace
Real trajectory
Flight Attitude 2: tilted
c (i)
(ii)
(iii)